**ADVANCED
FUNCTIONAL
MATERIALS**

Supporting Information

Multiphoton Absorption Stimulated Metal Chalcogenide Quantum Dot Solar Cells under Ambient and Concentrated Irradiance

Bo Hou, Byung-Sung Kim, Harrison Ka Hin Lee, Yuljae Cho, Paul Giraud, Mengxia Liu, Jingchao Zhang, Matthew L. Davies, James R. Durrant, Wing Chung Tsoi, Zhe Li, Stoichko D. Dimitrov,* Jung Inn Sohn,* SeungNam Cha,* and Jong Min Kim

Supplementary Materials

Multiphoton Absorption Stimulated Metal Chalcogenide Quantum Dot Solar Cells Under Ambient and Concentrated Irradiance

Bo Hou[1,‡], Byung-Sung Kim[2,‡,], Harrison K. H. Lee[3], Yuljae Cho[4], Paul Giraud[2], Mengxia Liu[5,§], Jingchao Zhang[6], Matthew L. Davies[3], James R. Durrant[3,7], Wing C. Tsoi[3], Zhe Li[8], Stoichko Dimitrov[9*], Jung Inn Sohn[10*], SeungNam Cha[11*] and Jong Min Kim[12]

1. Department of Physics and Astronomy, Cardiff University, Cardiff CF24 3AA, United Kingdom
2. Department of Engineering Science, University of Oxford, OX1 3PJ, Oxford, United Kingdom
3. SPECIFIC, College of Engineering, Swansea University, SA1 8EN, Swansea, United Kingdom
4. University of Michigan-Shanghai Jiao Tong University Joint Institute, Shanghai Jiao Tong University, 800 Dong Chuan Road, Minhang District, Shanghai 200240, China
5. Department of Electrical and Computer Engineering, University of Toronto, 10 King's College Road, Toronto, Ontario M5S 3G4, Canada
6. Department of Biostatistics and Bioinformatics, Emory University, Atlanta, GA, 30322, USA
7. Department of Chemistry, Imperial College London, SW7 2AZ, London, United Kingdom
8. School of Engineering and Materials Science (SEMS), Queen Mary University of London, E1 4NS, London, United Kingdom
9. School of Biological and Chemical Sciences, Queen Mary University of London, E1 4NS, London, United Kingdom
10. Division of Physics and Semiconductor Science, Dongguk University, Seoul 100-715, Republic of Korea
11. Department of Physics, Sungkyunkwan University, Suwon, 16419, Republic of Korea
12. Department of Engineering, University of Cambridge, CB3 0FA, Cambridge, United Kingdom

Corresponding authors:
Email: s.dimitrov@qmul.ac.uk
Email: junginn.sohn@dongguk.edu
Email: chasn@skku.edu
‡ These authors contributed equally to this work.
§ Present address: Cavendish Laboratory, University of Cambridge, J. J. Thomson Avenue, Cambridge, CB3 0HE, United Kingdom

Supplementary Contents:

SI. Microscopy analysis

The highly monodispersed feature of as-prepared PbS QDs is demonstrated from the bright-field transmission electron microscopy (BFTEM) on a JEOL JEM-3000F field emission gun TEM at 300 KV. The size of these particles is 2.8 ± 0.2 nm (Figure S1a). The specific cubic nature is evidenced by the cross-grating pattern that was captured by high-resolution BFTEM through [001] zone axis (Figure S1b).[1] These patterns are formed by the 45-degree crossing of the {200} and {220} planes, from which the lattice constant *a* can be directly extracted as 6.0±0.1 Å.[2]
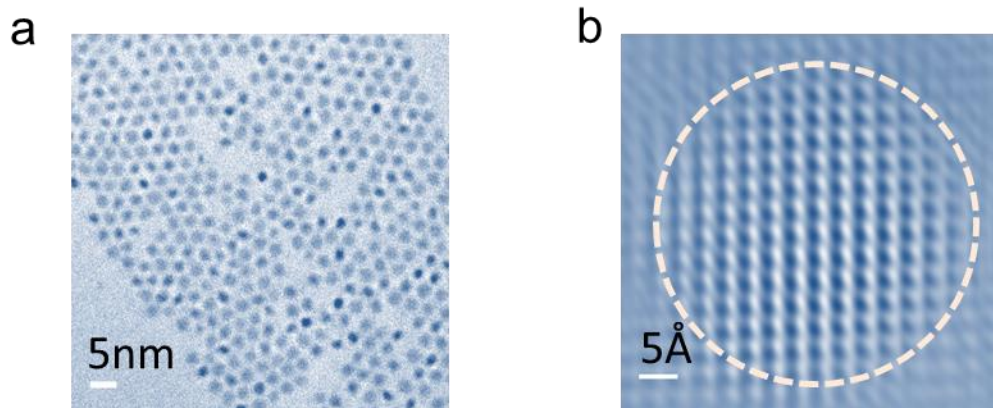
Figure S1. a, b) Bright-field TEM and atomic-scale HRTEM images of as-prepared PbS QDs.

SII. fs-Transient absorption analysis (fs-TAS)

The excitation fluence was estimated by recording the excitation pulse energy through fixed-size arises with a pyroelectric energy sensor (Ophir Photonics PE9). The charge densities in Figure 1g are calculated by dividing the maximum of the transient absorption bleach signal by the number of photons absorbed by the sample and the film thickness measured using a DektakXT.

a

b
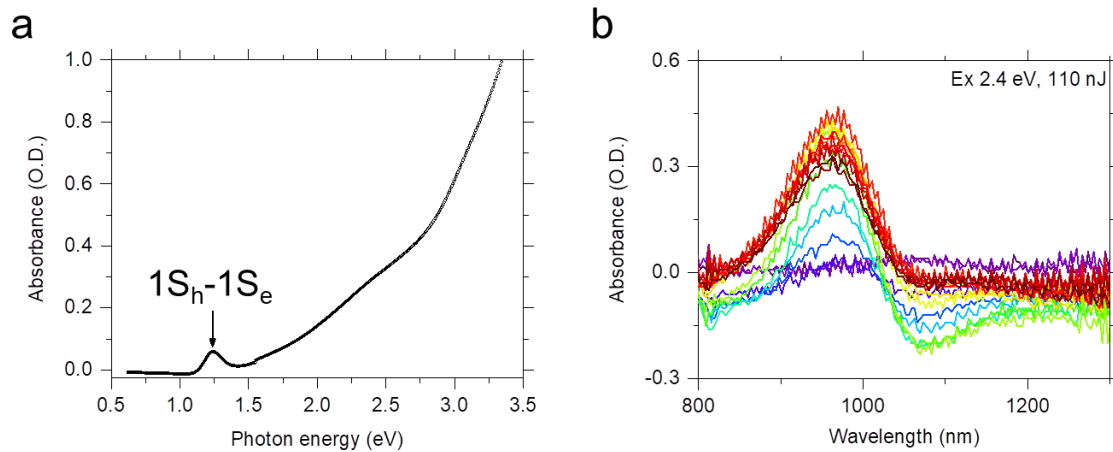
Figure S2. (a) Stationary absorption spectra of as-prepared PbS QDs. (b) Representative transient absorption spectra of PbS nanocrystals for a 2.4 eV excitation from 0.01 (purple&blue) to 6.5 nanoseconds (red&brown). All spectra recorded for different excitation intensities and wavelengths studied in this work showed similar spectral signatures and overall dynamics.
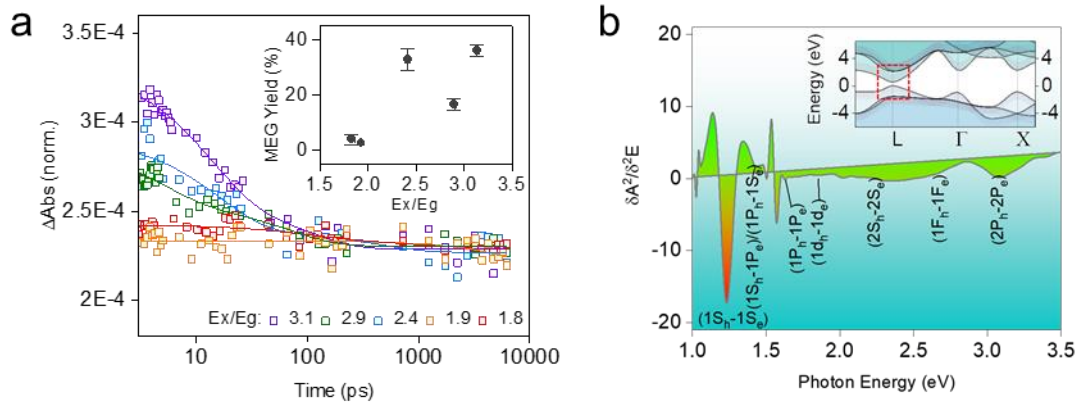
Figure S3. a, Exciton population decay dynamics recorded with different pump photon energies for the QD oleic acid solution demonstrating the presence of multi-exciton generation (MEG) in this sample. This is concluded from the appearance of picosecond Auger signal relaxation at Ex/Eg > 2, where Ex/Eg is the ratio of the excitation photon energy and QD's optical bandgap. The kinetics were recorded at excitation intensities that generated the same exciton fluences in the films. The solid lines are exponential fits to the data. The MEG yields were estimated from the ratio of the amplitude of the TA signal at 3.5 ps (when MEG is complete for all kinetics) and after 160 ps (when the Auger recombination process is complete and only single-exciton relaxation occurs).[3] The inset shows the MEG quantum yields as a function of Ex/Eg. The error bars correspond to the standard deviation of the transient absorption signal noise calculated from the residual of the exponential fits and the pump-energy measurements. b, Interband transition and excitonic peaks of 2.8 nm PbS QDs calculated based on the second derivative of its absorption spectrum. The inset of (b) shows a schematic representation of the DFT calculated the relativistic electronic-band structure of PbS QDs based on k·p perturbation theory.[3-5]
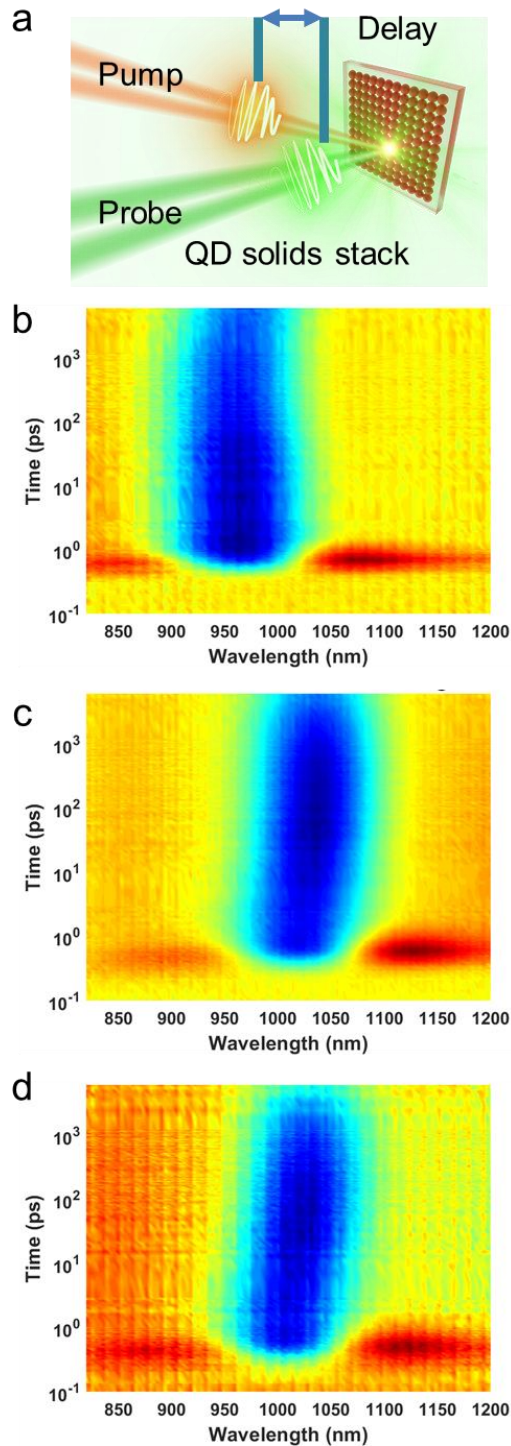
Figure S4. (a) A schematic for employing TAS to investigate the MPA process in solid QD films and devices. 3D $1S_e$-$1S_h$ bleach dynamics of films of (b) PbS-oleic acid (23.4 $\mu J.cm^{-2}$), (c) PbS-TBAI (6.4 $\mu J.cm^{-2}$) and (d) full devices (4.8 $\mu J.cm^{-2}$), recorded using transient absorption spectroscopy and an excitation wavelength of 526 nm. Peak shift for PbS-TBAI and full device result from charge thermalization through the density of states and indicate diffusion of charges through the films. Least square fitting of the peak shift of PbS-TBAI and full device with an exponential function gives 6.8 (±1.1) ps and 15.7 (±3.2) ps for thermalization process, while exponential fitting of the signal rise time gives 14.2 (±0.6) ps and 19.5 (±2.6) ps, respectively. The peak shift energy was calculated to be 21.9 meV (±0.9 meV) for PbS-TBAI film and 20.6 meV (±0.7 meV) for full devices, likely representative of the size dispersity of the prepared films.

SIII Indoor QDSC parameters

Representative indoor lamp spectra with 200 lux and 1000 lux illumination intensity are shown in Figure S5a, b respectively. There is a noticeable lumen counts enrichment (e.g., Figure S5b) can be observed when the illumination altered from 200 lux to 1000 lux. The indoor photostability was evaluated by exposing the QDSC under 1000 lux for 1824 hours. As shown in Figure S6 a-d, there is no noticeable device degradation can be detected. Moreover, a high photon flux induces a smaller shunt and series resistance was observed as illustrated in Figure S6 e-f. Detail QDSC indoor light-harvesting performance parameters are listed in Table S1.

The ideality factor of a diode, n, can be extracted from the light intensity dependent and dark diode curves.[6] The extracted plots and values of n are listed in Figure S7 and Table S2. The values of n usually vary between 1 and 2 depending on charge carrier dynamics. For instance, the n equals to 2 when the recombination current dominates, and n equals to 1 when the diffusion current dominates. When both currents are comparable, n has a value between 1 and 2.[7] Furthermore, we also note that analysis using different evaluating methods may yield slightly different ideality factor values, particularly in the case of under dark or light illumination.[8,9]
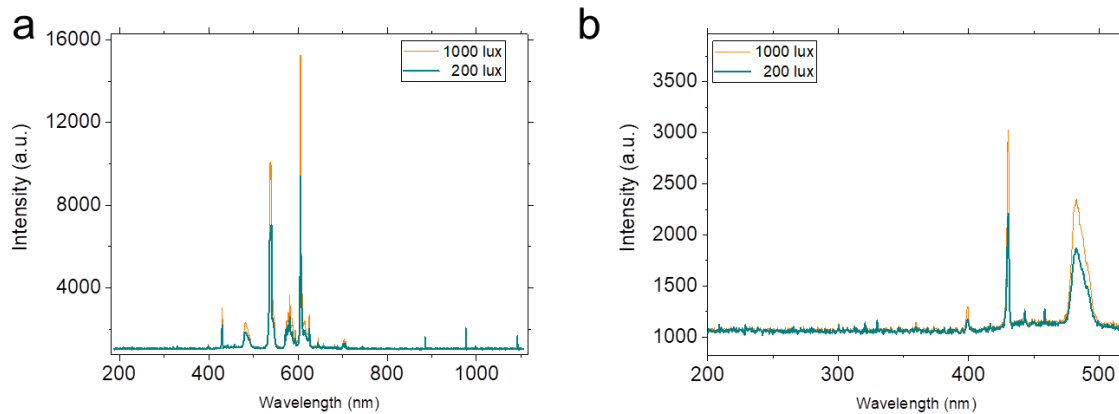
Figure S5. a) The spectra of the indoor lamp with 200 lux and 1000 lux illumination. b) An enlarged view of spectra with photon energy ranging from 200 nm to 520 nm.
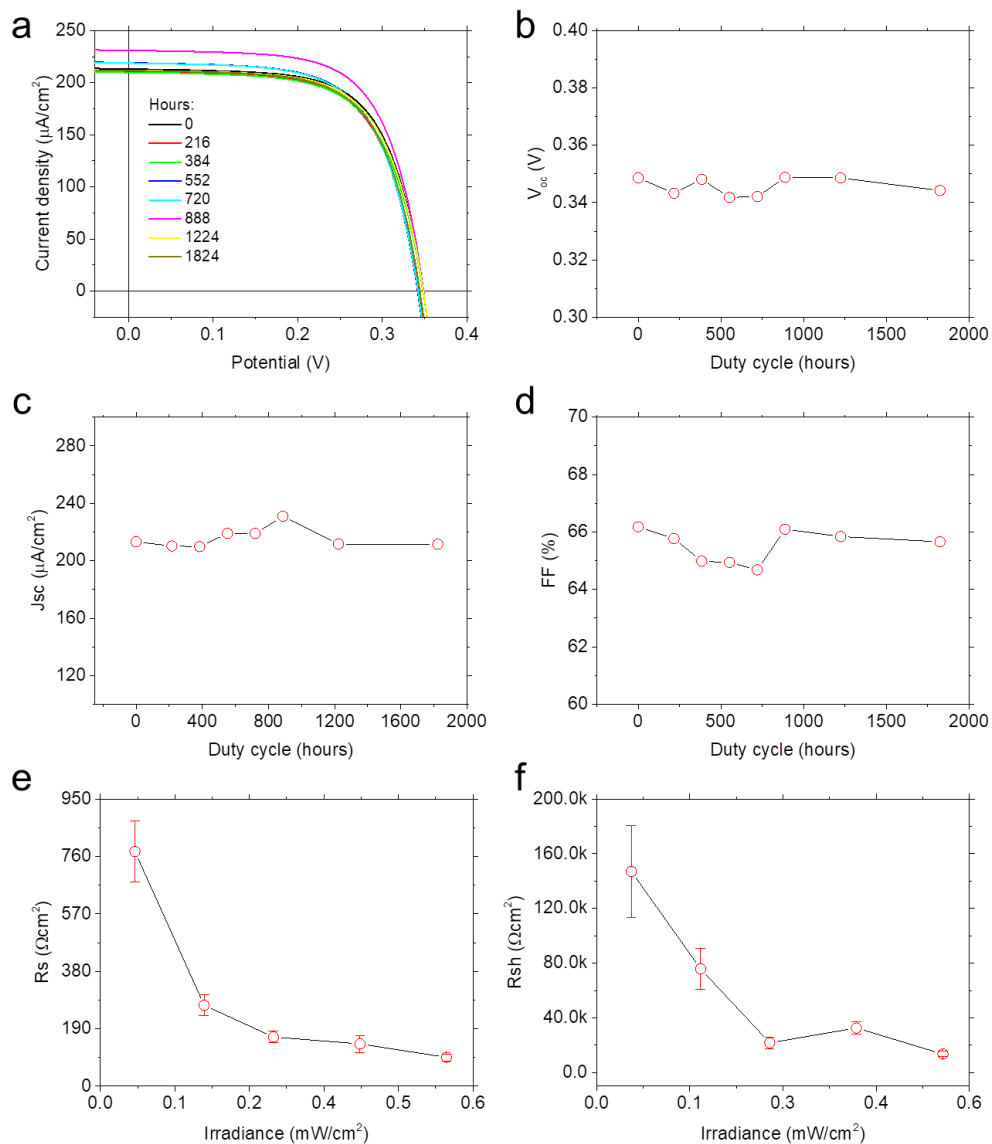
Figure S6. a) J-V curves of QDSC during 1824 hours 1000 lux indoor light exposure. V_{oc} b), J_{sc} c), FF d) evolution as a function of exposure time. e) and f) illustrate the evolution trend of R_s and R_{sh} as a function of irradiance respectively.

Table S1 Summary of indoor QD photovoltaic parameters				
200 Lux (0.0557 mWcm^{-2})	600 Lux (0.1672 mWcm^{-2})	1000 Lux (0.2787mWcm^{-2})	1500 Lux (0.4181mWcm^{-2})	2000 Lux (0.5574mWcm^{-2})
power conversion efficiency (PCE)				
14.9±0.3% (15.2)	17.0±0.3% (17.3)	17.8±0.3% (18.1)	18.4±0.3% (18.7)	19.2±0.3% (19.5)
fill factor (FF)				
66.2%	67.6%	69.0%	69.0%	69.4%
ideality factor (n)				
1.36	1.36	1.36	1.36	1.36
short circuit current density (J_{sc})				
44.6 µA/cm^2	130.9 µA/cm^2	213.3 µA/cm^2	315.3 µA/cm^2	423.8 µA/cm^2
open circuit voltage (V_{oc})				
0.28 V	0.32 V	0.34 V	0.35 V	0.36 V
series resistance (R_s)				
776.3 Ωcm^2	267.6 Ωcm^2	162.9 Ωcm^2	139.9 Ωcm^2	95.5 Ωcm^2
shunt resistance (R_{sh})				
147051.9 Ωcm^2	75777.7 Ωcm^2	21696.5 Ωcm^2	32584.9 Ωcm^2	13491.4 Ωcm^2
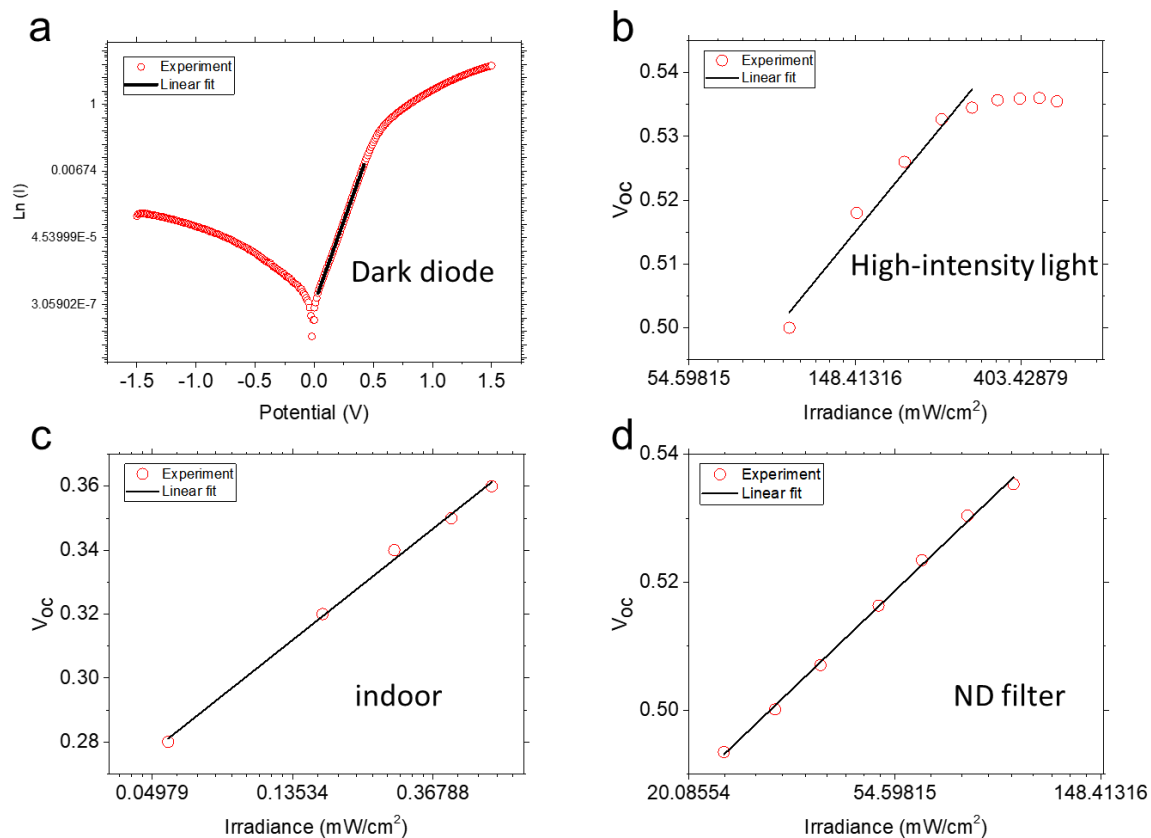
Figure S7. Plots for extraction the n factors such as semi-log dark diode curve a), different irradiance from high-intensity light b), various irradiance from ambient indoor light c), and different one Sun light intensity by employing ND filter d).

Table S2 Summary of ideality factor calculated from different conditions				
calculation condition	High-intensity light	Dark diode	Indoor low light	ND filter
ideality factor (n)	1.24	0.96	1.36	1.2

SIV Indoor PV and IR sensor IoT circuit design and parameters

Figure S8a describes the distance-dependent irradiance variation measurement results. It illustrates the feasibility of closely integrating QDSC with indoor illumination system to power sensors. J-V curves and QDSC-Sensor integration circuit design are shown in Figure S8b and c. By closely attach the QDSC with the indoor light system (e.g., Philips fluorescent light), an IR motion sensor can be sufficiently powered. Detail power, potential, and capacitance generation parameters during 1 hour indoor light illumination are listed in Table S3.
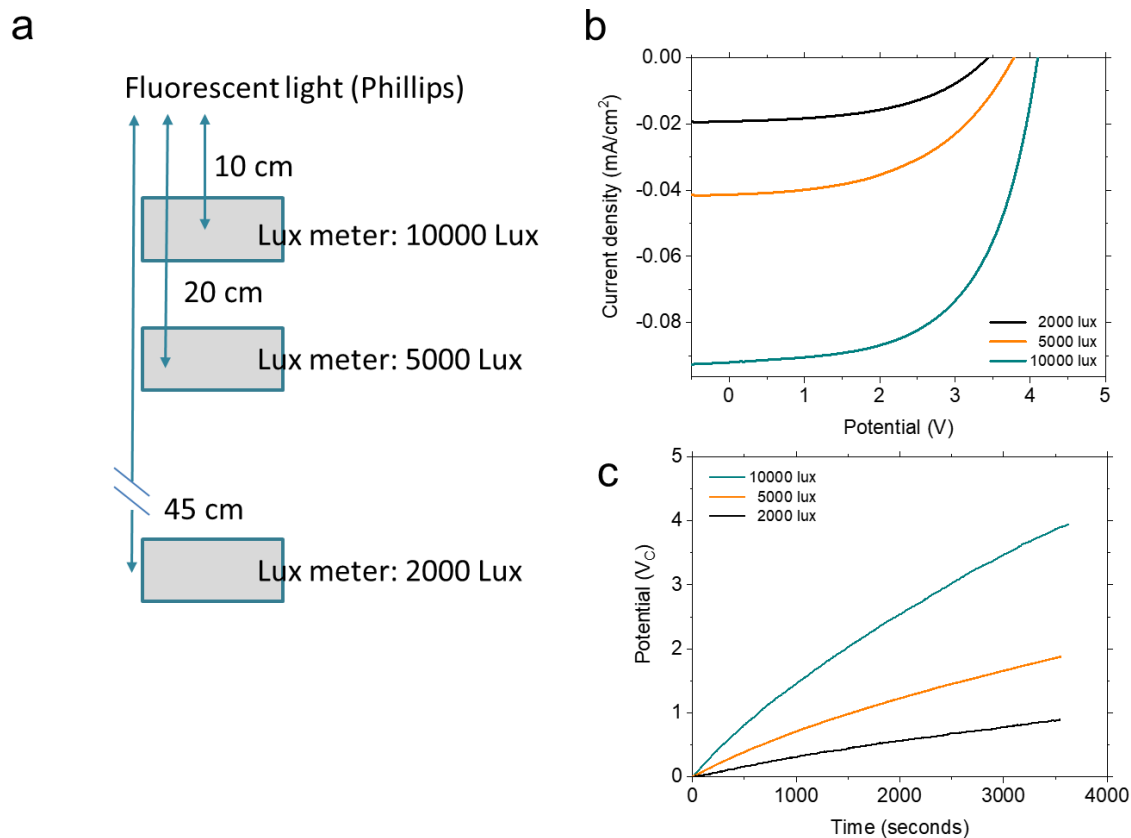
Figure S8. a) The distance-dependent irradiance variation. It should be noted that we simulate the indoor experiment as close as the usual ambient lighting conditions in an office.[6] Because we only focus on obtaining the targeting flux number (such as 2000 lux), therefore, all the lights in the office are switched on. The distance-dependent irradiance variation looks like linear, which is because of the contribution from different light sources. b) J-V curve of QDSC under different indoor irradiance. c) Real-time potential measurement in capacitors (20 mF) which was charged by QDSC under different indoor irradiance.

Table S3 One hour indoor QDSC charging parameters					
Light Intensity [Lux]	Capacitance [mF]	Potential [V]	Q [mC]	Energy [mJ]	Power [uW]
2000	10	1.36	13.6	9.25	2.57
	20	0.63	12.6	6.30	1.75
	30	0.48	14.4	3.46	0.96
5000	10	2.35	23.5	27.61	7.67
	20	1.3	26	16.90	4.69
	30	0.74	22.2	8.21	2.28
10000	10	3.68	36.8	67.71	18.81
	20	2.63	52.6	69.17	19.21
	30	1.47	44.1	32.41	9.00

SV High light QDSC parameters.

The QDSCs were evaluated by high standard AAA class solar simulator system (Figure S9) under a solar concentration from 1 Sun to 30 Suns.

Due to the elevated surface temperature, a noticeable efficiency drop can be observed as shown in Figure S10a (sample A and sample B). Therefore, a low concentration condition (i.e., 1-5 Suns) as highlighted in Figure S10a was employed in the rest of our manuscript. Figure S10b exhibit the general efficiency trend of QDSCs (sample 1 to sample 18) under the solar concentration of 1 to 5 Suns. All the samples showed only small efficiency drop when the solar concentration was increased. Figure S10c and Figure S10d provide more evidence of efficiency evolution trend as a function of solar concentration with multiple time measurements. It indicates that QDSC can sustain a high solar irradiance without noticeable efficiency degradation.

In the range of 1 to 5 Suns, the power conversion efficiency can also be enhanced due to the enrichment of photon flux. As the integration results are shown in the Figure S11a, the number of photons with a wavelength between 280 nm to 500 nm can be dramatically enriched when the solar concentration adjusts from 1 Sun to 5 Suns. The detail J-V and power output curves are provided in Figure S11b, Figure S11c, and Figure S11d.

The power output and maximum power point (MPP) voltage ratio (e.g., essential parameters for evaluating commercial PV products) are extracted and reported in Figure S12a.[6,10] We determined the 'constant MPP ratio' from our QDPV based on a fractional-voltage methodology which was reported to be an effective way for prospecting PV under viable light modulation.[6,11] Solar cell power conversion efficiency (η) is calculated from equation $\eta = \frac{FF \times J_{sc} \times V_{oc}}{P_{in}} \times 100\%$, where J_{sc} denotes short-circuit current density, FF denotes fill factor, V_{oc} denotes open circuit voltage and P_{in} denotes photon flux power input.[12] In practice, without a perfect cell cooling system, the increasing carrier densities and illumination flux will lead to a high dark current density and high cell temperature which inevitably result in the decline of photo conductivity.[12,13] Therefore, though the J_{sc} displays a proportional enlargement, the FF is showing a fast accession, saturation and degeneration trend which subsequently cause deviation of a linear efficiency enhancement (Figure S12b).[12]

By using a differential resistance approach, the series resistance and shunt resistance of QDSC under different irradiance can also be extracted (Figure S13).[2] There is a noticeable decline trend in the parasitic cell resistance, and it is slowing down in the high solar concentration ratio. Moreover, a high photon flux induces a smaller shunt and series resistance was observed which is consistent with the results extracted from indoor light

QDSC as shown in Figure S6 e-f. The parameters of QDSC under different solar concentration, including power conversion efficiency, fill factor, ideality factor, short circuit current density, open circuit voltage, series resistance, shunt resistance are summarised in the Table S4.
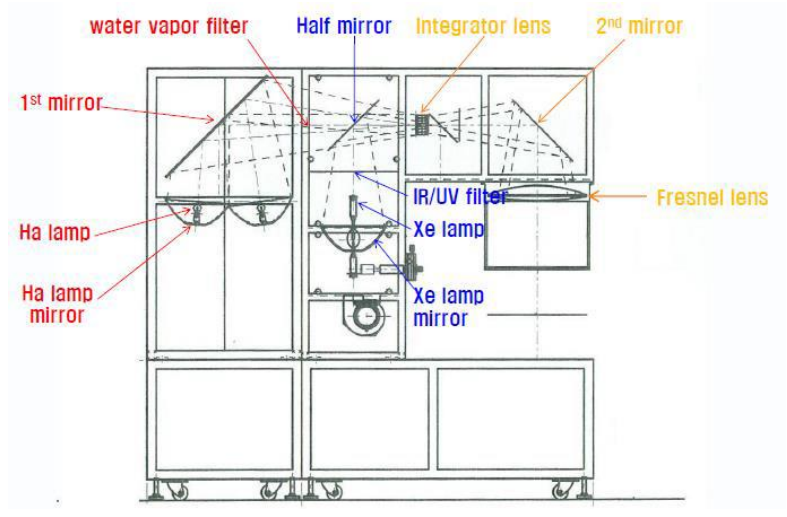
Figure S9. A chart of the concentrated solar simulator system.
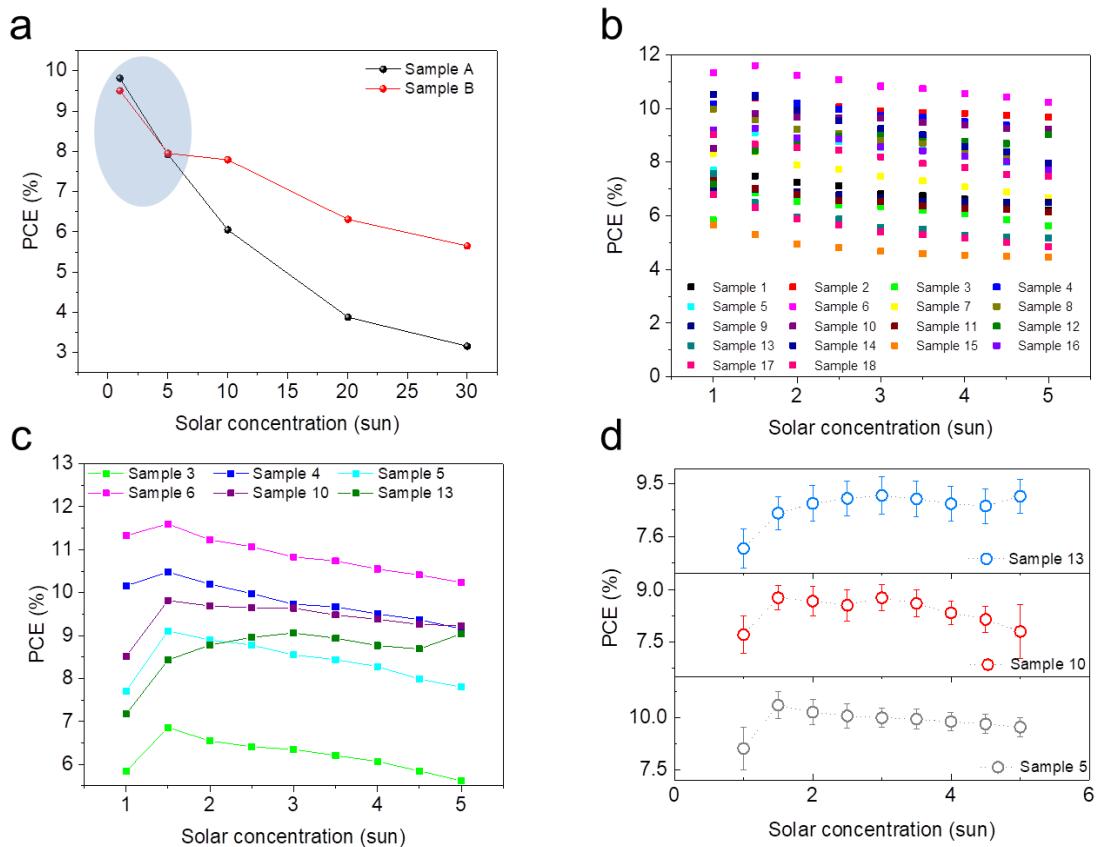
Figure S10. QDSC PCE evolution as a function of solar concentration a) 1~30 Suns, b) 1~5 Suns. Ellipsoidal shade area highlighted the concentration of interest- 1 to 5 Suns low concentration region. c, d) Additional selected QDSC PCE evolutions as a function of solar concentration 1~5 Suns. The error bar in (d) was generated from multiple measurements.
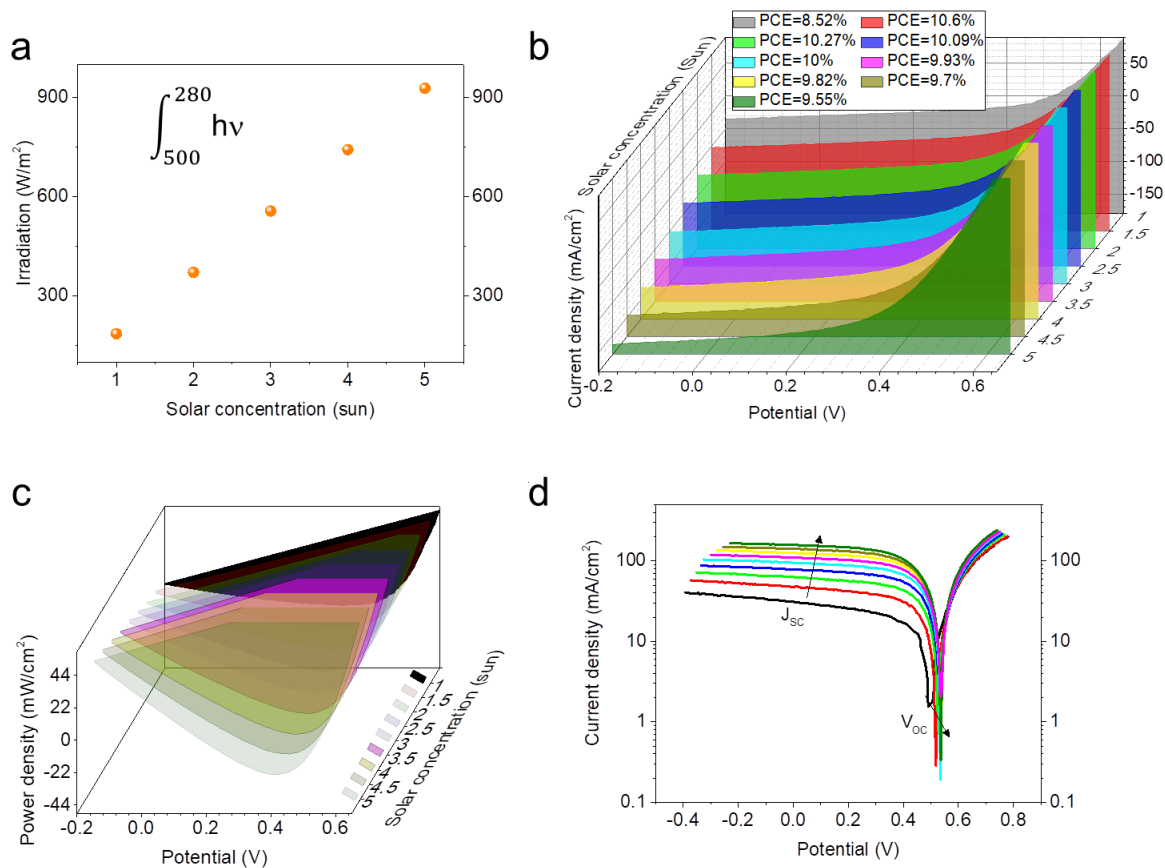
Figure S11. a) Integration of total irradiance between photon wavelengths of 280 to 500 nm. b) J-V curves of a typical QDSC under different solar concentration. c) The power density of QDSC under different solar concentration. d) Semi-log J-V plots of QDSC under different solar concentration.
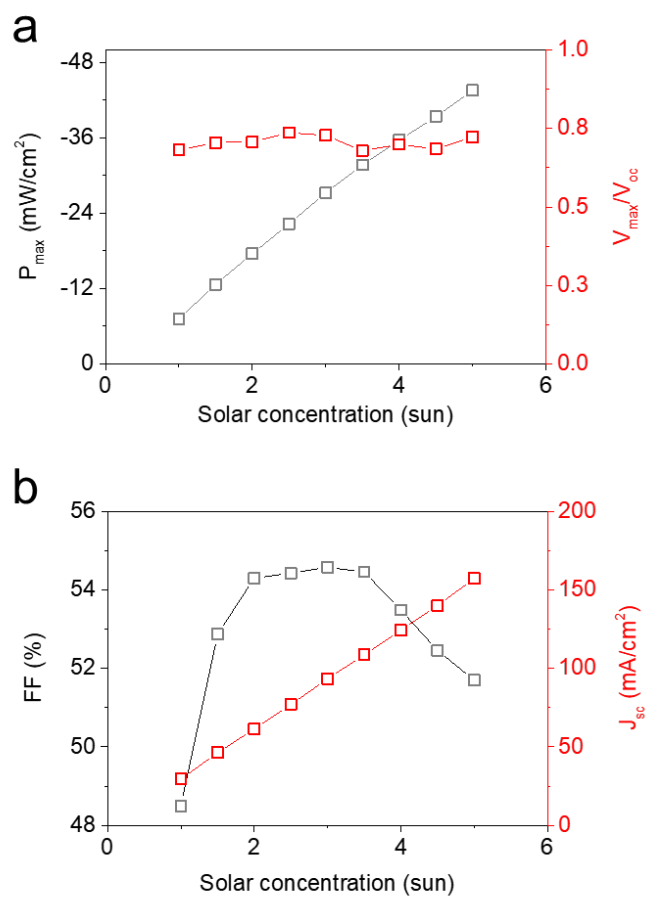
Figure S12. a) The MPP point and Vmax to V_{OC} ratio at different solar concentration. b) The evolution of FF and Jsc as a function of solar concentration.
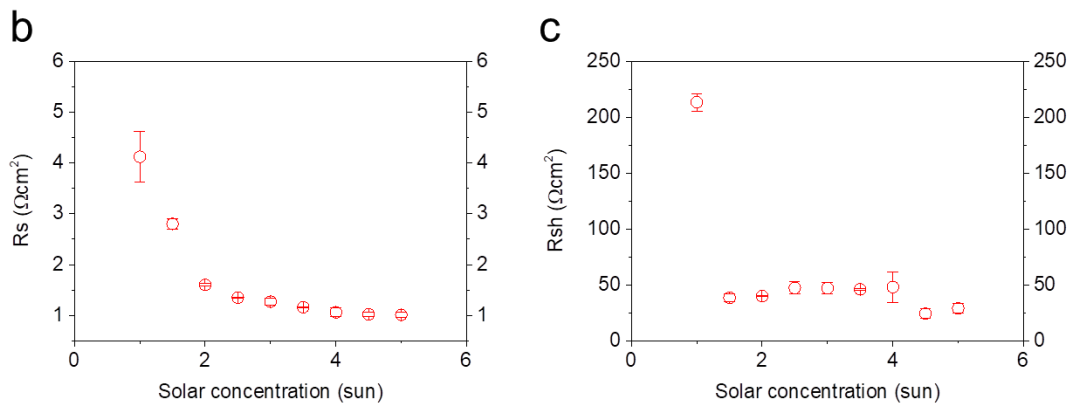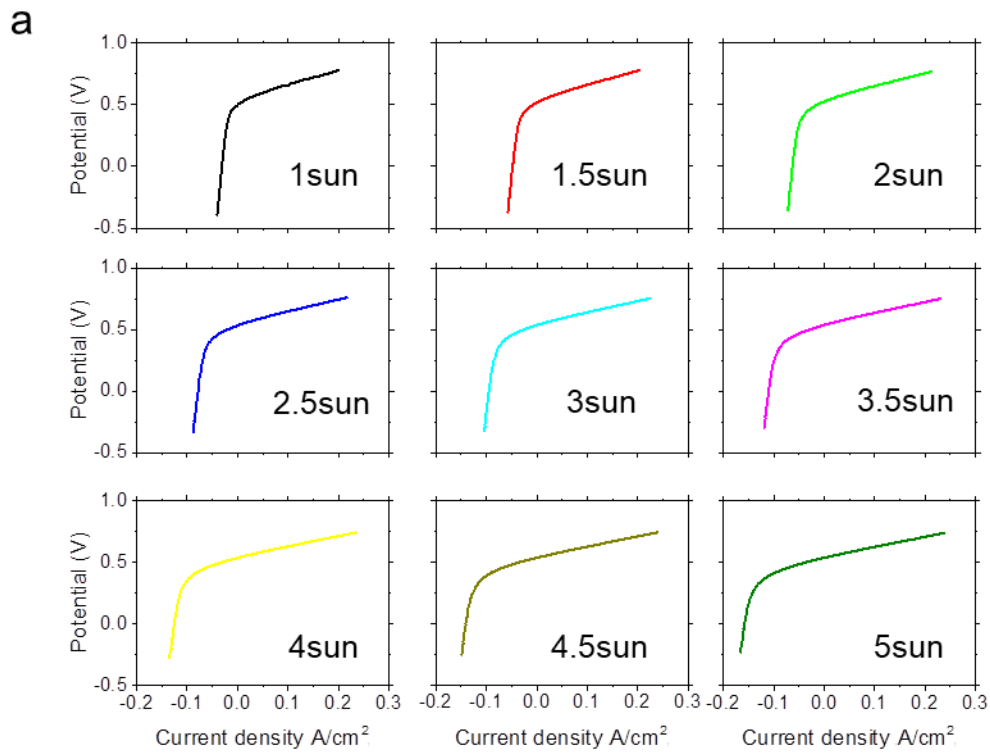
Figure S13. a) V-J curves of QDSC under different solar concentrations which were used for extracting series resistance (*Rs*) and shunt resistance (*Rsh*). b,c) Rs and Rsh evolution as a function of solar concentration.

Table S4 Summary of low-concentration QD photovoltaic parameters (1-3 Suns)					
	1 Sun (100 mWcm^{-2})	1.5 Suns (150 mWcm^{-2})	2 Suns (200 mWcm^{-2})	2.5 Suns (250 mWcm^{-2})	3 Suns (300 mWcm^{-2})
power conversion efficiency (*PCE*)	8.52±1.03% (9.55)	10.6±0.65% (11.25)	10.27±0.6% (10.87)	10.09±0.58% (10.67)	10.0±0.48% (10.48)
fill factor (*FF*)	48.5%	52.87%	54.3%	54.43%	54.58%
ideality factor (*n*)	0.82	0.82	0.82	0.82	0.82
short circuit current density (*J$_{sc}$*)	29.55 mA/cm^2	46.27 mA/cm^2	61.46 mA/cm^2	76.95 mA/cm^2	93.45 mA/cm^2
open circuit voltage (*V$_{oc}$*)	0.5 V	0.52 V	0.53 V	0.53 V	0.54 V
series resistance (*R$_s$*)	4.12±1.5 Ωcm^2	2.8±1.1 Ωcm^2	1.6±0.03 Ωcm^2	1.35±0.01 Ωcm^2	1.27±0.07 Ωcm^2
shunt resistance (*R$_{sh}$*)	213.3±7.7 Ωcm^2	38.47±3.6 Ωcm^2	40±0.2 Ωcm^2	47.3±5.6 Ωcm^2	47.07±4.9 Ωcm^2

	3.5 Suns (350 mWcm^{-2})	4 Suns (400 mWcm^{-2})	4.5 Suns (450 mWcm-^{2})	5 Suns (500 mWcm^{-2})
Continue Table S4 summary of low-concentration QD photovoltaic parameters (3-5 Suns)				
power conversion efficiency (*PCE*)	9.93±0.48% (10.41)	9.82±0.45% (10.27)	9.7±0.45% (10.15)	9.545±0.46% (10.01)
fill factor (*FF*)	54.46%	53.49%	52.46%	51.7%
ideality factor (*n*)	0.82	0.82	0.82	0.82
short circuit current density (*J$_{sc}$*)	108.65 mA/cm^2	124.35 mA/cm^2	140.05 mA/cm^2	157.35 mA/cm^2
open circuit voltage (*V$_{oc}$*)	0.54 V	0.54 V	0.54 V	0.54 V
series resistance (*R$_s$*)	1.16±0.01 Ωcm^2	1.06±0.09 Ωcm^2	1.02±0.05 Ωcm^2	1.01±0.05 Ωcm^2
shunt resistance (*R$_{sh}$*)	46.05±0.59 Ωcm^2	48.08±23.64 Ωcm^2	24.20±4.2 Ωcm^2	28.94±4.28 Ωcm^2

SVI Polymer lens concentrator

Figure S14 a-e present the detail information about polymer lens concentrator simulations and detail parameters used in the simulations are listed in the Table S5.[14] Figure 14f shows the power output curve of as-prepared QDSC integrated with different polymer lens. The optical absorption spectra of QD solid film together with a polymer lens are shown in Figure S15a. The first exciton peak remains very well after covering by the polymer lens caption which indicates exciton dynamics of QD film did not alter when the light rays were converged. The photostability of QD concentrator PV (QDCPV) is evaluated by 6 hours continuous 1 sun insolation. As shown in Figure S15b-f, there is no significant device performance degradation during light exposure. Detail QDCPV device parameters are summarised in Table S6.
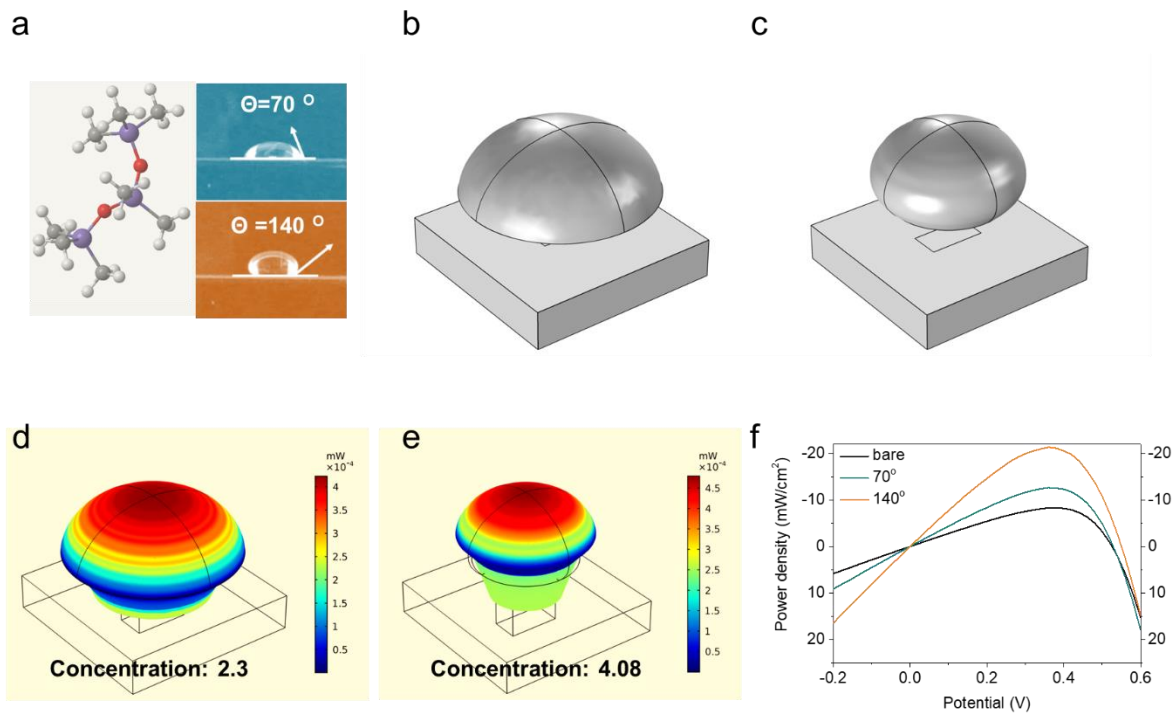
Figure S14. a) The molecule configuration of PDMS monomer and two CCD images of polymer lenses with different contact angles. 3D geometric profiles of 70° b) and 140° c) lens and simulated concentration ratios (d, e) employed for polymer solar concentrator. f) Power output curve of as-prepared QD polymer lens CPVs.

Table S5 Parameters for polymer lens concentrator simulation		
	70°	140°
Total emitted power density (mW/cm^2)	100	100
Total received power density (mW/cm^2)	102.91	106.68
Active area power density (mW/cm^2)	231.03	408.97
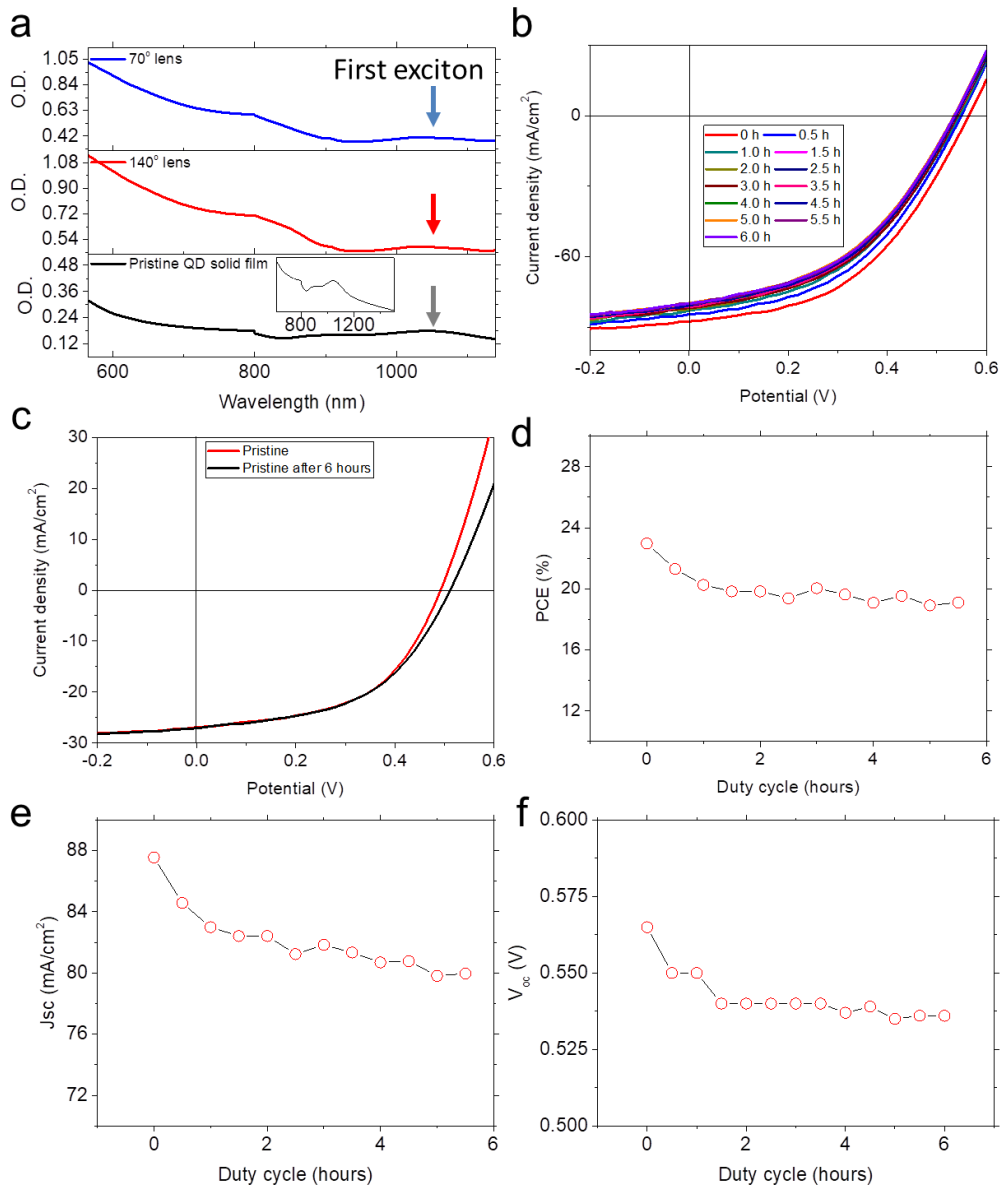
Figure S15. a) Optical absorption of QD solid film, QD solid film capped by 70° and 140° polymer lens. b) J-V curves of QDCPV capped by 140° polymer lens for 6 hours 1 Sun irradiance. c) J-V curves of QDCPV before and after 6 hours of light exposure. PCE d), J_{sc} e) and V_{oc} f) evolution trend as a function of exposure time.

Table S6 Summary of polymer lens QD photovoltaic parameters			
	Pristine QDSC	70° lens	140° lens
Module power conversion efficiency (*MPCE*)	8.31%	12.6%	21.3%
fill factor (*FF*)	0.56	0.54	0.49
Module short circuit current density (*MJ$_{sc}$*)	28.42 mA/cm^2	44.56 mA/cm^2	79.99 mA/cm^2
open circuit voltage (*V$_{oc}$*)	0.52 V	0.52 V	0.54 V
series resistance (*R$_s$*)	3.84 Ωcm^2	2.9 Ωcm^2	2.21 Ωcm^2
shunt resistance (*R$_{sh}$*)	337.52 Ωcm^2	141.2 Ωcm^2	27.9 Ωcm^2

SVII Water lens concentrator

Mixers of H_2O and ethanol were used to generate different curvature water drops on a hexamethyldisilazane (HMDS) modified glass substrate (reverse side of ITO) to mimic the function of the solar concentrator. Figure S16 (a-d) shows a series of water lens with different ethanol volume concentration on hexamethyldisilazane (HMDS)-modified glass. It is well known that the wettability of a surface can be modified by the adsorption of the ethanol molecules on a liquid-vapor and liquid-solid interface.[15,16] The increased ethanol concentration changed the wettability of the HMDS-modified surface, resulting in a decreased wetting angle of water lens. Therefore, by adding these solution drops on the top of QDSC, artificial QD CPV can be easily fabricated. These water-based QD CPV show photon energy harvesting enhancement as exhibited in Figure S16e, which produce prominent power output comparing to bare QDSC (Figure S16f). Detail water-based QDCPV device parameters are summarised in Table S7.
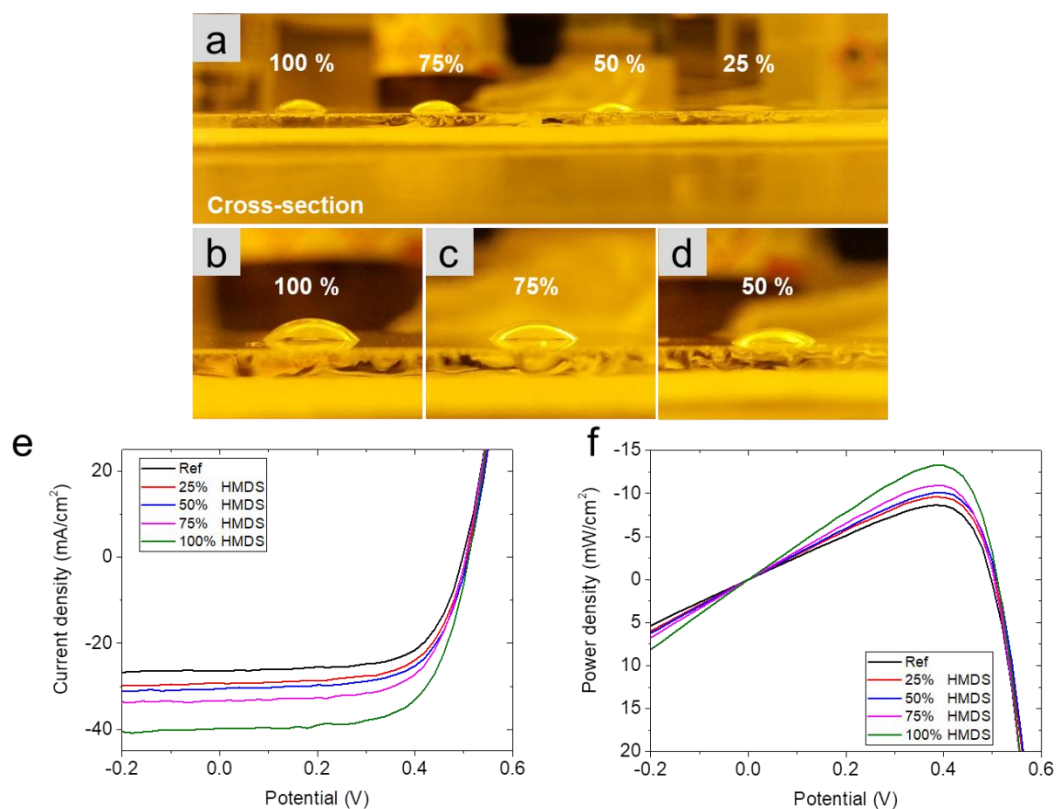
Figure S16. a) Cross-section view images of water drops having a different amount of ethanol on HMDS treated ITO substrate. b-c) enlarged CCD cross-section images. *J-V* e) and *P-V* f) curves of water-based QD CPVs.

Table S7 summary of water lens QD photovoltaic parameters					
	Pristine QDSC	25%	50%	75%	100%
module power conversion efficiency (*MPCE*)	8.64%	9.60%	10.10%	10.92%	13.28%
fill factor (*FF*)	0.6553	0.6554	0.6629	0.6555	0.6423
short circuit current density (J_{sc})	26.38 mA/cm^2	29.31 mA/cm^2	30.48 mA/cm^2	33.33 mA/cm^2	39.76 mA/cm^2
open circuit voltage (V_{oc})	0.50 V	0.50 V	0.50 V	0.50 V	0.52 V
series resistance (R_s)	2.25 Ωcm^2	2.37 Ωcm^2	2.42 Ωcm^2	2.06 Ωcm^2	1.49 Ωcm^2
shunt resistance (R_{sh})	171.35 Ωcm^2	529.43 Ωcm^2	246.19 Ωcm^2	181 Ωcm^2	179.48 Ωcm^2

SVIII A summary of the state-of-the-art PbS QD solar cells

Table S8 A summary of the state-of-the-art PbS QD solar cells						
Fabrication method	Irradiance	Jsc (mA/cm^2)	Voc (V)	FF (%)	PCE (%)	Reference
Solution-state ligand exchange	1 sun	29.1	0.64	70	13	[17]
Solution-state ligand exchange	1 sun	29.5	0.64	66	12.5	[18]
Solution-state ligand exchange	1 sun	30.2	0.65	68	13.3	[19]
QD/OPV hybrid	1 sun	29.6	0.66	67	13.1	[20]
Solution-state ligand exchange	1 sun	26.1	0.53	58.1	8.1	[21]
Solution-state ligand exchange	IR region	3.2	0.43	65.2	0.9	[21]
Solid-state ligand exchange	1 sun	25.2	0.61	59	9.1	[22]
Solid-state ligand exchange	1 sun	21.9	0.635	51	7.0	[23]
Solid-state ligand exchange	1 sun	25.3	0.633	66.8	10.4	[23]
Solid-state ligand exchange	IR region	3.44	0.32	61	0.67	[24]
Solid-state ligand exchange	1 sun	25.84	0.63	68.8	11.21	[25]
Solid-state ligand exchange	1 sun	29.55	0.5	48.5	8.52±1.03 (9.55)	This work
Solid-state ligand exchange	Indoor (2000 Lux)	0.4238	0.36	69.4	19.2±0.3 (19.5)	This work
Solid-state ligand exchange	1.5 sun	46.27	0.52	52.87	10.6±0.65 (11.25)	This work
Solid-state ligand exchange	Polymer lens (4.08 sun)	79.99	0.54	49	21.3	This work

SIV Universal irradiance QDSC performance in different latitudes

The simulated QDSC performance among Hilo, Palm Springs, Seattle, Juneau are based on their hourly statistics annual irradiance data which were extracted from USA National Renewable Energy Laboratory (NREL) National Solar Radiation Database 1991–2010 as listed in the Table S8. We simulate our QDSC performance from actual daily irradiance among various latitudes (LA) to further quantify the emerging use of QDSCs under the different light conditions. By using a least squares algorithm, the polynomial from these variables (J_{sc}, V_{oc}, PCE) can be determined and empirical regression equations correlated to the PCE (Figure S17) can be computed (solid fitting lines). Therefore, given different LA insolation, the PV power can be readily simulated. It should be noted that these approximations are based on a constant FF (mean value 58.4%) and incident flux independent dark current condition.[6,12] As shown in Figure 4c, mean daily annual solar irradiance as a function of the month from four different USA cities are selected. These four towns (Hilo, Palm spring, Seattle and Juneau) have represented latitude degrees across the northern hemisphere.[26] It can be seen that there is a clear daily solar irradiance difference between these latitudes and they are all deviated from one Sun condition. However, as highlighted from the periphery of the contour map of Figure 4c, when we superimpose our QDSC into these cities, a similar PCE can be obtained regardless of the LA difference.

Furthermore, simulated indoor QDSC power generation between 7pm-24pm among these four cities as a function of irradiance is shown in Figure S18. Furthermore, QDSC measurement protocols are provided in Figure S19 and Table S9. These protocols were used for evaluating QDSC performance and stability under sunlight, indoor-light, and high-intensity light irradiance.
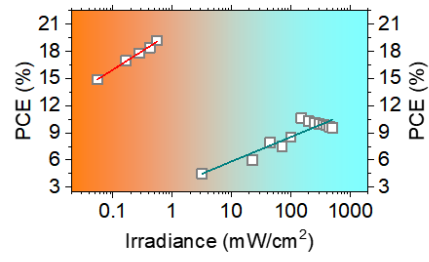
Figure S17. Least squares algorithm fitted lines for PCE evolution under variable ambient (indoor) and solar (sunlight, high light) irradiance.

Table S9 Annual hourly based solar irradiance (mW/cm^2) Hilo, Hawaii, Latitude: 19.717, Longitude: -155.05, TZ:-10																							
Time \\ Month	0	1	2	3	4	5	6	7	8	9	10	11	12	13	14	15	16	17	18	19	20	21	22	23
January	0	0	0	0	0	0	0	5.8	21.3	38.2	54	60.3	63.1	62.1	50.8	34.2	20.2	4.2	0	0	0	0	0	0
February	0	0	0	0	0	0	0.1	6.8	22.6	41.9	58.7	70	68.6	68.8	56.6	40.6	24.5	9.8	0.3	0	0	0	0	0
March	0	0	0	0	0	0	0.5	9.9	25.1	41.2	56.9	66.3	68.2	63.2	55.8	41	25.4	12.5	0.5	0	0	0	0	0
April	0	0	0	0	0	0	3.4	16.3	33.6	51.6	63.5	76.3	77.7	75.2	63.1	51.3	28.8	13.1	0.6	0	0	0	0	0
May	0	0	0	0	0	0.1	7.5	23.5	40.5	62.7	68.9	78.9	77.4	77.1	58.4	44.8	33.5	14.4	1.7	0	0	0	0	0
June	0	0	0	0	0	0.2	7.2	21.7	36	56.2	76.8	78.4	86.2	84.5	71.2	55.5	34.6	15.8	2.8	0	0	0	0	0
July	0	0	0	0	0	0.1	6.3	20.1	41.1	60	73.7	83	80.8	81.4	71.6	56.6	39.4	20.2	4	0	0	0	0	0
August	0	0	0	0	0	0	4	21.2	33.9	53.8	75.6	85	85.8	83.9	78	60	37.7	16.9	1.8	0	0	0	0	0
September	0	0	0	0	0	0	3.2	18.8	37.2	57.1	74	78.9	85.4	81	71.6	52.6	32	10	0.3	0	0	0	0	0
October	0	0	0	0	0	0	1.3	13.4	30.5	43.3	53.5	68.7	65	65.8	51.4	35.5	19.4	3.3	0	0	0	0	0	0
November	0	0	0	0	0	0	0.5	12.5	28.7	43.3	58.3	60.8	56.5	55.3	44.6	30.9	16	1.2	0	0	0	0	0	0
December	0	0	0	0	0	0	0.1	8	24	38.5	46.3	53.7	55	50.4	42.9	27.2	14.4	1.4	0	0	0	0	0	0
January	0	0	0	0	0	0	2.8	14.8	31.2	49	63.3	71.7	72.5	70.7	59.7	44.2	27.2	10.2	1	0	0	0	0	0

Time / Month	0	1	2	3	4	5	6	7	8	9	10	11	12	13	14	15	16	17	18	19	20	21	22	23
\多列Continue Table S9 Annual hourly based solar irradiance (mW/cm^2) Palm Springs, CA, Latitude: 33.833˚, Longitude: -116.5˚, TZ:-8																								
January	0	0	0	0	0	0	0.1	8.1	24.4	35.7	46.6	53	50.6	44.1	32.6	19.1	3.7	0	0	0	0	0	0	0
February	0	0	0	0	0	0	0.7	13.4	29.9	47	59	67.4	68.9	58.5	47.4	31.2	12.9	0.7	0	0	0	0	0	0
March	0	0	0	0	0	0.1	8.1	28.7	48.6	65.9	78	81.7	81	74.7	60.3	42.7	22.8	3.3	0	0	0	0	0	0
April	0	0	0	0	0	2.4	19.6	41.3	62.4	78.9	89.9	95.5	91	84.1	68.4	52.6	29.2	9.4	0.2	0	0	0	0	0
May	0	0	0	0	0.2	9	29.1	50.6	70.2	85.5	92.2	99.5	97	90.7	76.8	58.1	36.2	15.5	1.3	0	0	0	0	0
June	0	0	0	0	0.5	11.6	32.2	52.8	71.4	86.8	97.1	100.4	100.2	92.8	80	62.5	41.1	20.3	2.9	0	0	0	0	0
July	0	0	0	0	0.1	7.9	25.1	46.5	64.2	77.2	86.4	95.3	96.2	87.3	75.7	60.3	40.2	19.5	2.7	0	0	0	0	0
August	0	0	0	0	0	3.2	21.7	43.1	62.7	78.4	88.8	95.2	93.4	84	72.5	55.3	33.8	12.2	0.8	0	0	0	0	0
September	0	0	0	0	0	0.6	15.8	36.3	55.8	72.7	82.2	86.1	83.5	75.6	61.5	42.6	20.4	3	0	0	0	0	0	0
October	0	0	0	0	0	0.1	8.4	26.5	46.9	61.1	68.3	71.3	66.5	59.2	44.8	27	7.3	0.2	0	0	0	0	0	0
November	0	0	0	0	0	0	2.1	19.1	36.7	51.2	58.3	63.2	59.2	49	35.5	17.6	1.8	0	0	0	0	0	0	0
December	0	0	0	0	0	0	0.3	9	22.7	36.1	43.7	45.9	44.5	38.7	26.5	13.4	1.2	0	0	0	0	0	0	0
January	0	0	0	0	0.1	2.9	13.6	31.3	49.7	64.7	74.2	79.5	77.7	69.9	56.8	40.2	20.9	7	0.7	0	0	0	0	0

| Time \ Month	0	1	2	3	4	5	6	7	8	9	10	11	12	13	14	15	16	17	18	19	20	21	22	23
January	0	0	0	0	0	0	0	0	2.8	8.7	12.6	15.6	15.3	14.7	10.3	6.9	0.9	0	0	0	0	0	0	0
February	0	0	0	0	0	0	0	1.5	10.7	19	26.2	31.6	29.1	29.4	24	18.9	7.7	0.6	0	0	0	0	0	0
March	0	0	0	0	0	0	1	8.7	18.9	27.9	35.4	41.2	40.8	41.2	32.6	24.5	15.2	5.6	0.2	0	0	0	0	0
April	0	0	0	0	0	0.9	7.8	17.5	27.5	37	43.4	43.8	48.6	47.7	37.4	30.6	22.5	11.2	2.5	0	0	0	0	0
May	0	0	0	0	0.2	4.1	13.8	26	36.2	46.7	54.1	56.3	52.9	50.1	47.3	40.7	27.5	19.2	8	0.6	0	0	0	0
June	0	0	0	0	0.6	5.5	16.8	26.6	34.9	46.6	53	54.8	58.8	54.4	54.5	44.4	30.4	19.9	11.6	2.7	0	0	0	0
July	0	0	0	0	0.2	5.6	15.4	25.7	39.1	49.9	56.9	70.3	76.4	71.2	65.9	58	45.2	29.9	14.3	2.9	0	0	0	0
August	0	0	0	0	0	1.5	9.7	20.7	32.4	41.5	52.2	62.5	66.5	63.3	58.1	50.1	35.4	19.9	5.7	0.2	0	0	0	0
September	0	0	0	0	0	0.1	3.9	13.3	19.8	28.6	34.7	40.3	47.2	40.6	35.5	28.1	17.5	6.1	0.3	0	0	0	0	0
October	0	0	0	0	0	0	0.5	8	18.7	27.3	33.6	35.4	31.3	30.7	25.5	15.7	5.6	0.3	0	0	0	0	0	0
November	0	0	0	0	0	0	0	1.3	7.9	12	16.7	17	16.7	15.2	11.8	5.6	0.4	0	0	0	0	0	0	0
December	0	0	0	0	0	0	0	0	3.5	9	11.9	16.8	17.1	13.8	10.2	4	0.1	0	0	0	0	0	0	0
January	0	0	0	0	0.1	1.5	5.7	12.4	21	29.5	35.9	40.5	41.7	39.4	34.4	27.3	17.4	9.4	3.6	0.5	0	0	0	0

Continue Table S9 Annual hourly based solar irradiance (mW/cm^2) Seattle Boeing Field, WA, Latitude: 47.68˚, Longitude: -122.25˚, TZ:-8

Time / Month	0	1	2	3	4	5	6	7	8	9	10	11	12	13	14	15	16	17	18	19	20	21	22	23
Continue Table S9 Annual hourly based solar irradiance (mW/cm^2) Juneau INT'L ARPT, AK, Latitude: 58.35˚, Longitude: -134.583˚, TZ:-9																							
January	0	0	0	0	0	0	0	5.8	21.3	38.2	54	60.3	63.1	62.1	50.8	34.2	20.2	4.2	0	0	0	0	0	0
February	0	0	0	0	0	0	0.1	6.8	22.6	41.9	58.7	70	68.6	68.8	56.6	40.6	24.5	9.8	0.3	0	0	0	0	0
March	0	0	0	0	0	0	0.5	9.9	25.1	41.2	56.9	66.3	68.2	63.2	55.8	41	25.4	12.5	0.5	0	0	0	0	0
April	0	0	0	0	0	0	3.4	16.3	33.6	51.6	63.5	76.3	77.7	75.2	63.1	51.3	28.8	13.1	0.6	0	0	0	0	0
May	0	0	0	0	0	0.1	7.5	23.5	40.5	62.7	68.9	78.9	77.4	77.1	58.4	44.8	33.5	14.4	1.7	0	0	0	0	0
June	0	0	0	0	0	0.2	7.2	21.7	36	56.2	76.8	78.4	86.2	84.5	71.2	55.5	34.6	15.8	2.8	0	0	0	0	0
July	0	0	0	0	0	0.1	6.3	20.1	41.1	60	73.7	83	80.8	81.4	71.6	56.6	39.4	20.2	4	0	0	0	0	0
August	0	0	0	0	0	0	4	21.2	33.9	53.8	75.6	85	85.8	83.9	78	60	37.7	16.9	1.8	0	0	0	0	0
September	0	0	0	0	0	0	3.2	18.8	37.2	57.1	74	78.9	85.4	81	71.6	52.6	32	10	0.3	0	0	0	0	0
October	0	0	0	0	0	0	1.3	13.4	30.5	43.3	53.5	68.7	65	65.8	51.4	35.5	19.4	3.3	0	0	0	0	0	0
November	0	0	0	0	0	0	0.5	12.5	28.7	43.3	58.3	60.8	56.5	55.3	44.6	30.9	16	1.2	0	0	0	0	0	0
December	0	0	0	0	0	0	0.1	8	24	38.5	46.3	53.7	55	50.4	42.9	27.2	14.4	1.4	0	0	0	0	0	0
January	0	0	0	0	0	0	2.8	14.8	31.2	49	63.3	71.7	72.5	70.7	59.7	44.2	27.2	10.2	1	0	0	0	0	0

Figure S18. Simulated QDSC indoor power generation between 7 pm to 24 pm.

SX Solar cell measurement protocols.
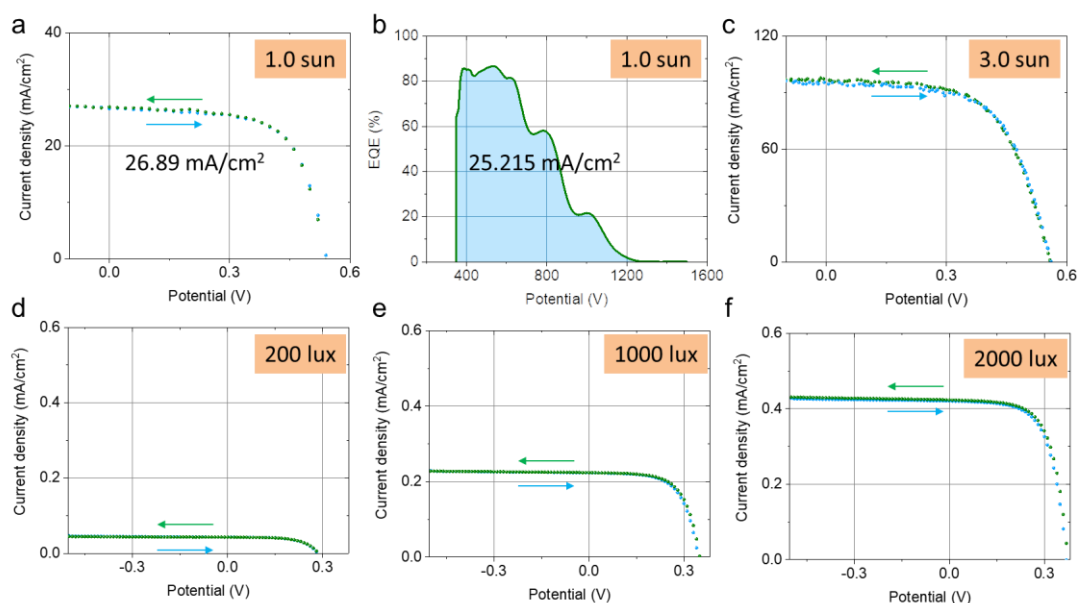
Figure S19. Test protocols of the QDSCs. Instantaneous forward and backward scanning J-V curves obtained under 1.0 Sun (a), 3.0 Sun (c), 200 lux (d), 1000 lux (e) and 2000 lux (f). Representative EQE spectrum provided in (b) was obtained with the same aperture mask for evaluating spectra and area mismatch (2.23 ± 0.91 mA/cm^2).[27] There is no considerable hysteresis effect observed in all QDSC devices under sunlight or indoor light. As widely reported, the QDSC generally show hysteresis-free and stable in air under sunlight.[28,29] Under high-intensity light irradiation, there is slightly hysteresis present due to thermal effect and the only backward scan is extracted for the rest of discussion.[30-32]

Table S10. Comparisons of the spectral mismatch between EQE and solar simulator

system.[27]

J_{sc} (mA/cm^2)	J_{sc} (EQE) (mA/cm^2)	Mismatch (mA/cm^2)
27.55 ± 1.15	25.32 ± 1.43	2.23 ± 0.91

Reference

1   Hou, B. *et al.* Structure and Band Edge Energy of Highly Luminescent CdSe1–xTex Alloyed Quantum Dots. *J. Phys. Chem. C* **117**, 6814-6820 (2013).

2   Hou, B. *et al.* Highly Monodispersed PbS Quantum Dots for Outstanding Cascaded-Junction Solar Cells. *ACS Energy Lett.* **1**, 834-839 (2016).

3   Ellingson, R. J. *et al.* Highly Efficient Multiple Exciton Generation in Colloidal PbSe and PbS Quantum Dots. *Nano Lett.* **5**, 865-871, doi:10.1021/nl0502672 (2005).

4   Kang, I. & Wise, F. W. Electronic structure and optical properties of PbS and PbSe quantum dots. *J. Opt. Soc. Am. B* **14**, 1632-1646 (1997).

5   Wei, S.-H. & Zunger, A. Electronic and structural anomalies in lead chalcogenides. *Phys. Rev. B* **55**, 13605-13610 (1997).

6   Lee, H. K. H., Li, Z., Durrant, J. R. & Tsoi, W. C. Is organic photovoltaics promising for indoor applications? *Appl. Phys. Lett.* **108**, 253301 (2016).

7   Memming, R. *Semiconductor Electrochemistry*. (Wiley, 2015).

8   Cowan, S. R., Roy, A. & Heeger, A. J. Recombination in polymer-fullerene bulk heterojunction solar cells. *Phys. Rev. B* **82**, 245207 (2010).

9   Kirchartz, T., Deledalle, F., Tuladhar, P. S., Durrant, J. R. & Nelson, J. On the Differences between Dark and Light Ideality Factor in Polymer:Fullerene Solar Cells. *J. Phys. Chem. Lett.* **4**, 2371-2376 (2013).

10   Husain, M. A., Tariq, A., Hameed, S., Arif, M. S. B. & Jain, A. Comparative assessment of maximum power point tracking procedures for photovoltaic systems. *Green Energy Environ.* **2**, 5-17 (2017).

11   Mathews, I., Kelly, G., King, P. J. & Frizzell, R. in *2014 IEEE 40th Photovoltaic Specialist Conference (PVSC).* 0510-0513.

12   Nelson, J. *The Physics of Solar Cells*. (Imperial College Press, 2003).

13   Sacco, A. *et al.* Dye-sensitized solar cell for a solar concentrator system. *Solar Energy* **125**, 307-313 (2016).

14   Jeter, S. M. Calculation of the concentrated flux density distribution in parabolic trough collectors by a semifinite formulation. *Solar Energy* **37**, 335-345 (1986).

15   Vázquez, G., Alvarez, E., Rendo, R., Romero, E. & Navaza, J. M. Surface Tension of Aqueous Solutions of Diethanolamine and Triethanolamine from 25 °C to 50 °C. *J. Chem. Eng. Data* **41**, 806-808 (1996).

16   Yonemoto, Y. & Kunugi, T. Experimental and theoretical investigation of contact-angle variation for water–ethanol mixture droplets on a low-surface-energy solid. *Int. J. Heat Mass Transfer* **96**, 614-626 (2016).

17   Biondi, M. *et al.* A Chemically Orthogonal Hole Transport Layer for Efficient Colloidal Quantum Dot Solar Cells. *Adv. Mater.* **32**, 1906199, doi:10.1002/adma.201906199 (2020).

18   Sun, B. *et al.* Ligand-Assisted Reconstruction of Colloidal Quantum Dots Decreases Trap State Density. *Nano Lett.* **20**, 3694-3702, doi:10.1021/acs.nanolett.0c00638 (2020).

19   Choi, M.-J. *et al.* Cascade surface modification of colloidal quantum dot inks enables efficient bulk homojunction photovoltaics. *Nat. Commun.* **11**, 103, doi:10.1038/s41467-019-13437-2 (2020).

20   Baek, S.-W. *et al.* Efficient hybrid colloidal quantum dot/organic solar cells mediated by near-infrared sensitizing small molecules. *Nature Energy* **4**, 969-976, doi:10.1038/s41560-019-0492-1 (2019).

21   Kim, Y. *et al.* A Facet-Specific Quantum Dot Passivation Strategy for Colloid Management and Efficient Infrared Photovoltaics. *Adv. Mater.* **31**, 1805580, doi:10.1002/adma.201805580 (2019).

22   Hu, L. *et al.* Achieving high-performance PbS quantum dot solar cells by improving hole extraction through Ag doping. *Nano Energy* **46**, 212-219, doi:https://doi.org/10.1016/j.nanoen.2018.01.047 (2018).

23   Teh, Z. L. *et al.* Enhanced Power Conversion Efficiency via Hybrid Ligand Exchange Treatment of p-Type PbS Quantum Dots. *ACS Appl. Mater. Interfaces* **12**, 22751-22759, doi:10.1021/acsami.9b23492 (2020).

24   Bi, Y. *et al.* Infrared Solution-Processed Quantum Dot Solar Cells Reaching External Quantum Efficiency of 80% at 1.35 μm and Jsc in Excess of 34 mA cm−2. *Adv. Mater.* **30**, 1704928, doi:10.1002/adma.201704928 (2018).

25   Lu, K. *et al.* High-Efficiency PbS Quantum-Dot Solar Cells with Greatly Simplified Fabrication Processing via "Solvent-Curing". *Adv. Mater.* **30**, 1707572, doi:10.1002/adma.201707572 (2018).

26   The irradiance is collected from USA National Solar Radiation Database 1991–2010.

27   Data were extracted across 20 samples. The current density of EQE system was integrated under AM1.5G TILT (ASTM-G173-03) with solar cell mask area 0.012 cm2. Jsc = (Jsc-forward + Jsc-backward)/2.

28   Xu, J. *et al.* 2D matrix engineering for homogeneous quantum dot coupling in photovoltaic solids. *Nature Nanotechnology*, doi:10.1038/s41565-018-0117-z (2018).

29   Liu, M. *et al.* Hybrid organic-inorganic inks flatten the energy landscape in colloidal quantum dot solids. *Nat. Mater.* **16**, 258-263 (2017).

30   Yandt, M. D., Cook, J. P. D., Kelly, M., Schriemer, H. & Hinzer, K. Dynamic Real-Time I-V Curve Measurement System for Indoor/Outdoor Characterization of Photovoltaic Cells and Modules. *IEEE J. Photovolt.* **5**, 337-343, doi:10.1109/JPHOTOV.2014.2366690 (2015).

31   Gordon, J. M., Katz, E. A., Tassew, W. & Feuermann, D. Photovoltaic hysteresis and its ramifications for concentrator solar cell design and diagnostics. *Appl. Phys. Lett.* **86**, 073508, doi:10.1063/1.1862776 (2005).

32   Speirs, M. J. *et al.* Temperature dependent behaviour of lead sulfide quantum dot solar cells and films. *Energy Environ. Sci.* **9**, 2916-2924, doi:10.1039/C6EE01577H (2016).